Inverse Problem Approach for the underwater localization of Fukushima Daiichi fuel debris with fission chambers

Jonathan Dumazert, Romain Coulon, Frédérick Carrel, Adrien Sari, Cheick Thiam, Mathieu Trocmé, Q. Lecomte, Hassen Hamrita, Romuald Woo, Frédéric Lainé, et al.

Inverse Problem Approach for the underwater localization of Fukushima Daiichi fuel debris with fission chambers

J. Dumazert*[1], R. Coulon[1], F. Carrel[1], A.Sari[1], C. Thiam[2], M. Trocmé[1], Q. Lecomte[1], H. Hamrita[1], R. Woo[1], F. Lainé[1], C. Frangville[1], M. Bakkali[3], K. Boudergui[1], B. Krausz[4], R. Pissarello[4], R. Delalez[4]

[1]*CEA, LIST, Laboratoire Capteurs Architectures Electroniques, 91191 Gif-sur-Yvette, France.*
[2]*CEA, LIST, Laboratoire National Henri Becquerel, 91191 Gif-sur-Yvette, France.*
[3]*CEA, LIST, Département Métrologie, Instrumentation et Information, 91191 Gif-sur-Yvette, France.*
[4]*ONET TECHNOLOGIES, Nuclear Decommissioning, 26700, Pierrelatte, France.*

***Abstract* — Fuel debris have a distinct neutron signature that can be detected to locate the said debris in a damaged nuclear power plant. Neutron measurement in a damaged PCV environment is however submitted to severe deployments constraints, including a high-dose-rate gamma background and limited available space. The study was therefore oriented towards small fission chambers (FC), with U-235-enriched active substrates. To investigate the expected performance of the FC in various irradiation conditions, a numerical model of the detector head was built. We describe the elaboration and experimental calibration of the numerical model and the Monte Carlo study of the fission rate inside U-235 coatings per generated neutron. The evaluation of a representative calibration coefficient then allowed us to carry out a multi-parameter performance study of a FC underwater, aiming at computing an explicit response function linking, on the one hand, the activity and spatial distribution of neutron emitters in a water container, with, one the other hand, the expected count rates measured by a fission chamber as a function of its radial and axial position inside the water volume. The FC underwater behavior was subsequently corroborated by a measurement campaign on a FC response, set at different positions inside a water drum, as a function of its axial and radial distance to a Cf-252 neutron source attached near the center of the container. We finally present an approach in which fuel debris localization is defined as an Inverse Problem, solvable with a Maximum-Likelihood Expectation Maximization (ML-EM) iterative algorithm. The projector matrix is built by capitalization on the results of the previously consolidated numerical studies. The ML-EM was tested on simulated data sets with a varying number of active voxels. Our first results indicate that, for a thermal neutron flux in the order of 10 n.cm^{-2}.s^{-1} at the detector, originating voxels are identified with a spatial resolution in the radial plane in the order of 10 to 100 cm^2.**

***Index Terms* — Neutron localization. Fuel debris. Fission chamber. Inverse Problem.**

I. Introduction

Fuel debris localization forms a critical step in the decommissioning road map of damaged nuclear power plants, as illustrated by the necessity to remove the melted nuclear fuel from the Fukushima Daiichi units stricken by a tsunami in March 2011. In this case, the loss of cooling led to a heat increase in the reactor vessel, which eventually caused a core meltdown. The melted nuclear fuel subsequently drilled the reactor vessel and partly spread at the bottom of the Primary Containment Vessel (PCV). Now, despite its high intensity, gamma radioactivity does not provide a relevant signature for the localization of fuel debris in the PCV environment. Indeed, the position of volatile fission products, such as Cs-134 and Cs-137, is not necessarily bound to the position of uranium or plutonium isotopes belonging to the melted core (corium). Furthermore, a mapping based on gamma-ray spectrometry, and taking advantage of the mainly low-energy signature of actinides, is practically unmanageable. Indeed, the spectral signature would be severely distorted by water, and the ratio between gamma-ray activity from actinides and from fission products is highly unfavorable. On the contrary, fuel debris have a distinct neutron signature, mainly due to Cm-244, and slightly Pu isotopes. The issue of debris localization will thus be addressed, in the course of this paper, from the prospect of neutron detection and counting.

Neutron measurement in a damaged PCV environment is submitted to severe deployments constraints, including:

- the ability to operate with excellent gamma rejection under a gamma dose rate of 1000 Gy.h^{-1};
- the insurance of thermal, mechanical and radiation robustness up an integrated gamma dose of 1000 Gy;
- the limited available space (in the order of 10 to 100 cm^3) through the maintenance aperture.

The neutron detection limits that are aimed at, expressed in units of neutron flux (neutron per centimeter square per second, n.cm^{-2}.s^{-1} or nv), lie between 10^{-1} and 10^3 n.cm^{-2}.s^{-1}.

Such general specifications narrow down the range of viable technological solutions. Most detectors will indeed be dramatically impacted by an intense gamma background. As an illustration, reference publications indicate the possibility of operating He-3 proportional counters, which remain the gold standard in conventional applications, up to an order of 1 Gy.h^{-1} gamma dose rate, providing a degradation in sensitivity is acceptable [1]. Conversely, neutron measurement by material activation, though suitable in presence of an intense gamma background (as evidenced by the use of activation dosimeters in Nuclear Power Plants), must be discarded as it does not provide a real-time response of the detector head. Given this diagnosis,

our study of principle regarding a neutron detection system for the underwater localization of corium was oriented towards fission chambers (FC).

Fission chambers are based on neutron-induced fission reactions. The active part of this detector is made of an actinide substrate, with industrial references being fissile U-235 to detect slow neutrons and fertile U-238 for fast neutrons (research work being also carried out with more exotic substrates such as Pu-239, Np-237 or Pu-242 [2]). As the aimed measurement is to be performed in a water-filled PCV, neutrons are expected to be found essentially with a kinetic energy close to the one of thermal agitation at room temperature, which justifies our preliminary choice of studying U-235-enriched FC. Fission reactions thus produce two fragment fissions with summed energies close to 160 MeV: the first one is generally lost in the substrate layer and the second one exits from the layer and ionizes the neutral gas contained in the fission chamber. CEA has a long expertise in transferring its development to industrial partners, including the PHOTONIS reference French company for supplying FC [3]. The selection of a model in the product catalogue of the company must be made in accordance with a tradeoff between thermal neutron sensitivity and dimensions. We chose as a factor of merit (FOM) the time required for registering 10 counts under a 10^{-1} to 10^{3} $n.cm^{-2}.s^{-1}$ (nv) neutron flux. On this basis, CFUE32 and CFUF34 models, with specified sensitivities in the order of 10^{-3} cps/nv, reach the FOM cut-off within 10 s (upper flux) to 27.8 h (lower flux), which are compatible with realistic deployment purposes. In the meantime, these small-size FC have respective diameter times length dimensions equal to 7 × 150 mm (CFUE32) and 4.7 × 85 mm (CFUF34), hence matching the space limitations we notified *supra*.

The choice of existing industrial fission chambers, and their associated theoretical performances were exposed. To study the expected performance of FC in various irradiation conditions (neutron activity, surrounding environment, and distance), a numerical model of the detector head was built. In this paper, we describe the elaboration of the numerical model and the Monte Carlo study of the fission rate inside U-235 coatings per generated neutron. To convert this fission rate into an expected count rate, we ran an experimental calibration of our code with a commercial, CFUE32 fission chamber. The evaluation of a representative calibration coefficient then allowed us to carry out a multi-parameter performance study of a FC underwater. The objective of this simulation study was to compute a relevant and explicit response function linking, on the one hand, the activity and spatial distribution of neutron emitters in a water container (representative of the bottom-floor of a water-filled PCV), with, one the other hand, the expected count rates measured by a fission chamber as a function of its radial and axial position inside the water volume. We then undertook a measurement campaign on the evolution of response set at different positions inside a water drum. The experimental study of the influence of a water diffusion environment is indeed crucial, both to validate the FC underwater behavior, and to provide a first set of results in conditions as close as possible to the ones of *in-situ* deployment. We finally present an approach in which fuel debris localization is defined as an Inverse Problem, solvable with a Maximum-Likelihood Expectation Maximization (ML-EM) iterative algorithm. The projector matrix is built by capitalization on the results of the previous numerical studies, and the ML-EM was tested on simulated data sets with varying parameters. For a determined neutron activity, the simulations allowed us to compute the acquisition time required for a localization associated with a given spatial resolution.

II. Numerical model of the fission chamber: detail and experimental calibration

A. *Model of a CFUE32 fission chamber*

Different probabilistic, Monte Carlo codes are available for particle transport modelling, among which MCNP is a reference tool for neutron diffusion and capture [4]. The MCNP6.1 program simulates a complete history of every generated corpuscle, for both source terms and recoil products, until the kinetic energy falls below an adjustable threshold [5]. In this study, we considered the modelling of a standard fission chamber, commercialized by PHOTONIS France S.A.S. under the reference CFUE32. This product is a small-size FC with a stainless steel structure (Z2CN18.10, volumic mass 7.9 $g.cm^{-3}$) and two coatings of U-235-enriched oxide, one on the internal electrode and one on the external electrode. The space inside the inner electrode and between both electrodes is filled with 100-% pure Ar at 900 kPa pressure. As previously stated, CFUE32 fission chambers embody two U_3O_8-coatings with weight percentage of ^{235}U exceeding 90 %. These two coatings form two 56-mm-long converters of neutrons into ionizing fission products, from which drifting electron and ion pairs originate. The model of the sensor head has a total length of 85 mm [6]. Fig. 1a) and b) represent the MCNP6.1 simulation model built in this section as side view and top view respectively. Moritz1.23 software is used to view MCNP6.1 simulation files [7].

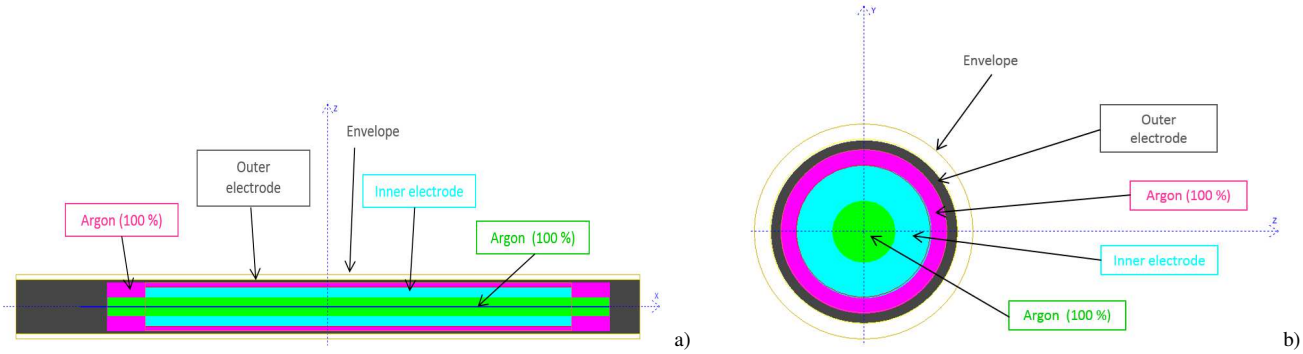

Fig. 1a) Side and b) top view of the MCNP6 model of a CFUE32 FC (Moritz 1.23).

B. *Model of the neutron moderation block*

Neutron diffusion is highly environment-sensitive, so that any experimental assessment of a FC neutron sensitivity should be conducted in a dedicated moderation block. The moderation block used for experimental calibration of the FC model, described in paragraph II.A, is a $104.8 \times 11.5 \times 26$ cm^3 High-Density Polyethylene (HDPE, formula CH_2, average volumic mass 0.95 g.cm^{-3}) parallelepiped, whose surface is covered by a 1-mm-thick coating of Cd, acting as a suppressor of slow neutrons (energy below 500 meV). We implemented a MCNP6 model of this block, using S(α,β) neutron transport data associated with polyethylene at 300 °K (material card: poly.10t). Indeed, neutron scattering is significantly impacted by molecular arrangements, especially in dense, hydrogenous materials such as polyethylene (or water). A set of five apertures with a diameter of 2.5 cm is present inside the MCNP6 model of the block, as illustrated in Fig. 2. In view of the comparative study between simulated and experimental neutron responses, the model of the CFUE32 FC is inserted at the center of the block along the *x*-axis, and in the closest row to the surface. The position of the barycenter of the so-inserted, modeled FC will be referred to as the *zero position* (0; 0; 0) in the rest of this section.

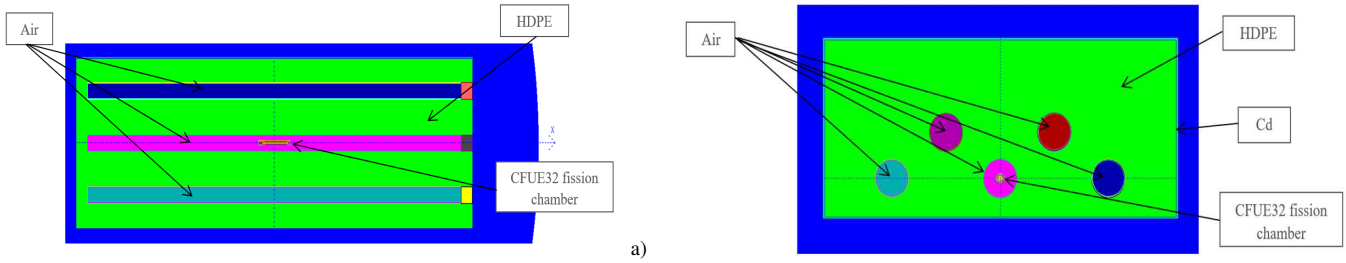

Fig. 2a) Side and b) cross-section view of a MCNP6 model of the neutron moderation block (Moritz 1.23).

C. *Experimental response of a CFUE32 fission chamber to reference neutron sources*

The experimental assessment of a CFUE32 neutron response was performed in the Neutron Irradiation Hall (NIH) of the Henri Becquerel National Laboratory (LNHB, CEA Saclay). The irradiation setup, including the FC and the moderation block, was housed in a blockhouse dedicated to the standardization of neutron sources under appropriate radiation protection conditions. The shielding is composed of a 1-cm-thick layer of stainless steel on both sides of a 40-cm-thick layer of concrete. The housing was included in the irradiation simulations that will be detailed in paragraph II.D. The experimental protocol is schematically represented in Fig.3a): the neutron source is positioned at the altitude h as the FC inside the block, and is screened along the *x*-axis. The experimental setup, with the distance-operated screening of the neutron source, is illustrated in Fig.3b). The neutron counting signal is recorded at positions $x = \{-10; 0; 10; 20; 30\}$ cm, that correspond to the longitudinal range of the remote controlled arm in the configuration. The FC is coupled with a 7820/7821 module (Mirion Technologies) providing the high-voltage supply (400 V) and pre-amplification. The voltage discrimination threshold (the fission product signal discriminated from the lower-energy gamma and alpha signal) is set equal to 450 mV. The absence of background count signal was validated over a 24-h integration time in the NIH.

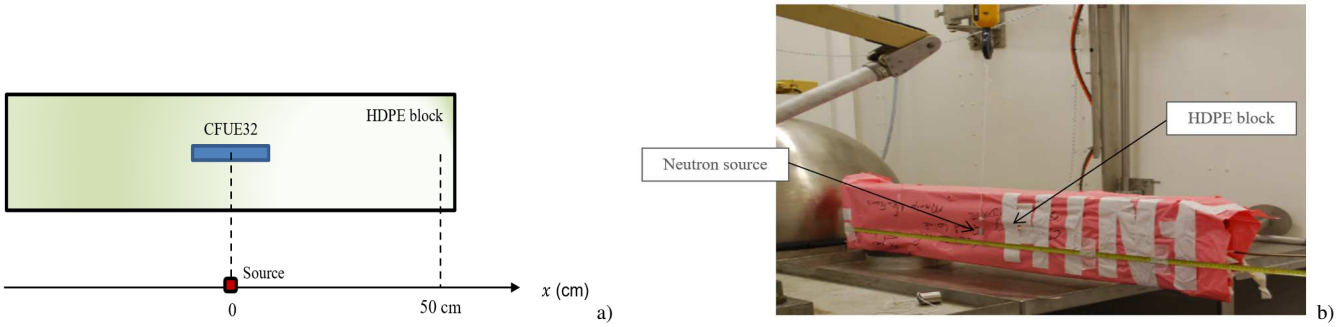

Fig. 3a) Schematic representation of the experimental protocol, and b) experimental setup with distance-operated screening of the neutron source.

The first experimental run was performed using an AmBe(α,n) source with a neutron emission rate $\upsilon_n = (2.080 \pm 0.027) \cdot 10^5$ n. s^{-1} at the measurement date.

To allow a quantitative comparison with simulation-based, expected values, the experimental neutron count rate, labelled $\lambda_n(x)$, is converted into a detection yield $Y_n(x)$ (expressed in count per neutron, c.n^{-1}) using the source neutron emission rate υ_n:

$$Y_n(x) = \frac{\lambda_n(x)}{\upsilon_n} \quad (1)$$

In order to provide data for an inter-comparison over different parameters other than the distance between neutron emitter and FC (*i.e.* source activity and type), two additional sets of counting experiments were carried out using:

- a second Am-Be source with a neutron emission rate $\upsilon_n = (6.36 \pm 1.91) \cdot 10^5$ n. s^{-1} at the measurement date;
- a Cf-252 spontaneous fission source with a neutron emission rate $\upsilon_n = (1.37 \pm 0.41) \cdot 10^5$ n. s^{-1} at the measurement date, and spectrum significantly different from the one of an Am-Be source.

For each source, the count rate λ_n was recorded at one or two different positions, matching reference positions from the previously described set of measurements:

- neutron source at 0 cm on the *x*-axis (Am-Be and Cf-252);
- neutron source + 20 cm on the *x*-axis (Am-Be).

D. Simulated response of a CFUE32 fission chamber to reference neutron sources

The simulation models of the CFUE32 FC and the moderation block were detailed in the previous paragraphs. A Monte Carlo simulation, performed with MCNP6.1, of the irradiation protocol described in paragraph II.C will give a neutron response for the sensitive volume of the FC, *i.e.* the two U_3O_8-coatings, relatively to the number of generated neutrons. The neutron emitter is modeled as a cylindrical volume source (5-mm diameter, 150-µm height) with isotropic and homogenous emission. Neutrons are generated according to a sampled reference spectrum tabulated in ISO 8592.2 [8]. The output parameter used to quantify the expected neutron response is the total fission rate $R_{(n,f)}(x)$ (expressed in fission per generated neutron, f.n^{-1}) inside both U_3O_8-coatings. The fission rate is accessed by using tally 4 (volumic particle fluence) of the MCNP6.1 code, with addition of SD4 (normalization) and FM4 (reaction rate, fissions: 18) cards. Evolution of the $R_{(n,f)}(x)$ as a function of the simulated Am-Be source position (center of mass) is shown in Fig. 4 against the evolution of $Y_n(x)$.

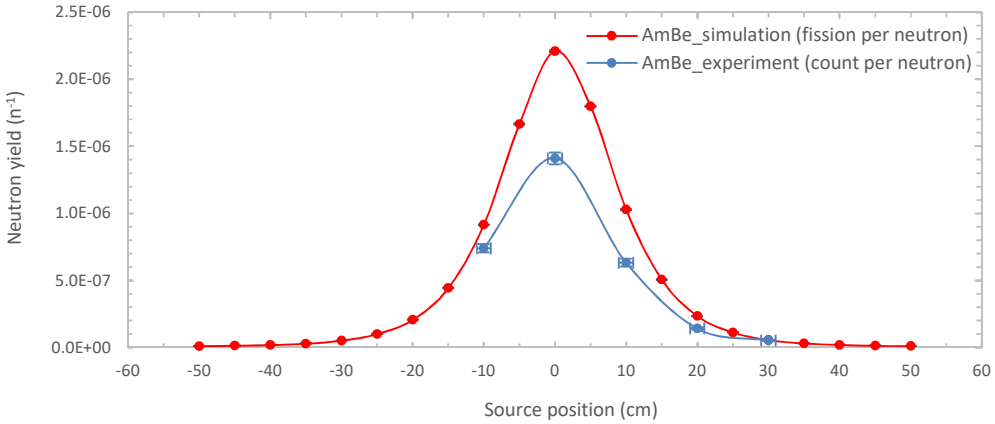

Fig. 4. Evolution of the experimental detection yield and the simulated fission rate as a function of source position (Am-Be).

Functions $R_{(n,f)}(x)$ and $Y_n(x)$ show an agreement in their trends: both distributions have a nearly Gaussian shape with a maximum at zero position. This concordance allows us to use the experimental data as a basis for the calculation of a calibration coefficient of the FC, which will be implemented in further simulations. The calibration coefficient is labeled $\omega_{(n,f)}(x)$ and expressed in count per fission (c.f^{-1}): it represents the average expected number of counts, for the acquisition setup, relative to one fission reaction inside the FC sensitive coatings. The loss of signal noted in Fig. 4 when comparing $R_{(n,f)}(x)$ and $Y_n(x)$ is mainly explained by:

- the stopping power of the oxide coating for the fission products inducing the signature of neutron reaction in the gaseous medium (effect known as self-absorption in the active layers);
- the voltage threshold set at 450 mV for alpha/neutron discrimination, cutting the lower-energy part of the reaction signature.

Point-by-point values for the calibration coefficient are derived as:

$$\omega_{(n,f)}(x) = \frac{Y_n(x)}{R_{(n,f)}(x)} \quad (2)$$

Over the five configurations of experimental acquisitions with the Am-Be reference source, we thus calculated a mean calibration coefficient $\bar{\omega}_{n,f} \pm \sigma(\omega_{n,f}) = 0.72 \pm 0.12\ \mathrm{c.f^{-1}}$ (at one standard deviation). Regarding the three complementary measurements described at the end of paragraph II.C, the conversion of count rates λ_n into detection yields Y_n were similarly performed, and the associated irradiation configurations were simulated to estimate fission rates $R_{(n,f)}$. The spectral distribution of Cf-252 radio-emitters was extensively studied in literature [9]. The model used in this simulation is based on a continuous Watt function with emission probability density described in Eq. (3) as a function of neutron energy E_n, and parameter settings $a = 1.025$ MeV and $b = 2.926\ \mathrm{MeV^{-1}}$ [10]:

$$f(E_n) \propto \exp\left(-\frac{E_n}{a}\right) \cdot \sinh(\sqrt{bE_n}) \quad (3)$$

The values obtained for Y_n and $R_{(n,f)}$ are reported in Table 1. We also calculated the associated calibration coefficients $\omega_{n,f}$, which all fall into the confidence interval $\bar{\omega}_{n,f} = 0.72 \pm 0.12\ \mathrm{c.f^{-1}}$ defined *supra* for Am-Be. The value $\bar{\omega}_{n,f}$ will then be retained to convert simulated fission rates into expected count rates on a CFUE 32 detection chain associated with a 450 mV threshold.

TABLE I. EXPERIMENTAL DETECTION YIELD, SIMULATED FISSION RATE AND CALIBRATION FACTOR FOR DIFFERENT SOURCE TYPES (AM-BE, CF-252), AND POSITIONS (0-20 CM)

Measurement \ Factor	Y_n **(c.n^{-1})**	$R_{(n,f)}$ **(f.n^{-1})**	$\omega_{(n,f)}$ **(c.f^{-1})**
Am-Be (0 cm)	$(2.04 \pm 0.08)\cdot10^{-6}$	$(2.59 \pm 0.03)\cdot10^{-6}$	0.78 ± 0.03
Am-Be (20 cm)	$(1.44 \pm 0.22)\cdot10^{-7}$	$(2.12 \pm 0.02)\cdot10^{-7}$	0.68 ± 0.10
Cf-252 (0 cm)	$(3.36 \pm 0.23)\cdot10^{-6}$	$(4.79 \pm 0.05)\cdot10^{-6}$	0.70 ± 0.05

A final simulation-based result is given by the calculation of a thermal neutron sensitivity estimate, associated with the Am-Be (0 cm) and the Cf-252 (0 cm) measurements. This estimate is labelled S_n and expressed in counts per neutron per square centimeter (c. $\mathrm{n^{-1}}$. $\mathrm{cm^2}$). The neutron fluence incident on the sensitive surface of the simulated FC is labeled Ψ_n and expressed in neutron n with energy below 500 meV per generated neutron $\mathrm{n_g}$ and square centimeter (n. $\mathrm{n_g^{-1}}$. $\mathrm{cm^{-2}}$). This fluence is estimated by using the average cell flux tally 4 of the MCNP6.1 code. An estimate of the neutron flux incident on the FC sensitive surface, labeled Φ_n (n. $\mathrm{cm^{-2}}$. $\mathrm{s^{-1}}$), is then derived by using the neutron emission rate as

$$\Phi_n = \Psi_n \cdot \upsilon_n \quad (4)$$

The neutron sensitivity estimate is ultimately calculated as

$$S_n = \bar{\omega}_{n,f} \cdot \frac{\lambda_n}{\Phi_n} \quad (5)$$

The derived values are respectively as $S_n = (8.3 \pm 0.5) \cdot 10^{-4}\,\mathrm{c.n^{-1}.cm^2}$ (Am-Be, 0 cm) and $S_n = (9.4 \pm 0.6) \cdot 10^{-4}\,\mathrm{c.n^{-1}.cm^2}$ (Cf-252, 0 cm). These results stand in excellent agreement with the CFUE32 fission chamber pulse-mode sensitivity to thermal neutrons, stated as equal to $10^{-3}\,\mathrm{c.n^{-1}.cm^2}$ in the manufacturer datasheet.

III. Simulation Study of a Fission Chamber Underwater Response: Impulse Function

The purpose of this simulation study was to compute a relevant response function linking, on the one hand, the activity and spatial distribution of neutron emitters in a water container (representative of the bottom-floor of a water-filled PCV), with, on the other hand, expected count rates measured by a fission chamber as a function of its position inside the water volume.

We used the calibrated validated FC model described in Section I as the detector, and the Watt spectrum of a Cf-252 point-like source as a neutron emitter. The choice of Cf-252 is justified by the fact that the isotope is a spontaneous fission source as Cm-244 that is to be detected in the Fukushima Daiichi scenario. Moreover, both fission spectra have mean neutron energies respectively equal to 2.11 MeV (Cm-244) and 2.13 MeV (Cf-252), close enough to consider the results of our study as representative of the expected neutron response to fuel debris [11]. The water container is modeled as a cylinder full of water surrounded by PMMA with an internal radius (water) equal to 27.5 cm and an external radius equal to 29 cm (water + PMMA). This model, on the one hand, matches the description of the tank that will be used in Section IV for the experimental counterpart of this study, and, on the other hand, by the limited range of fission neutrons into water, which will allow for a straightforward extrapolation of the results to any container. The rotational symmetry of the problem leads to a description of the expected response $Y_n(r,z)$, expressed in c.n^{-1} (using the mean calibration coefficient $\overline{\omega}_{n,f}$ to relate simulation-obtained fission rates to neutron responses) in a cylindrical r and z coordinate system.

The neutron source is simulated at $(0; 4.1\ \mathrm{cm})$ from the central bottom of the tank. The height corresponds to the center of mass of the active part of the FC model when the head of FC touches the bottom of the well (axial position labeled as $z = 0$). Radial position r of the center of mass of the FC active part is marked from the center of the circular bottom of the tank. We used the MCNP6.1 code to evaluate $Y_n(r,z)$ at discretized:

- $r = \{0.5; 3; 5.5; 8; 10.5; 13; 15.5; 18; 20.5; 23; 25.5\}$ cm radial positions, and
- $z = \{0; 2.5; 5; 7.5; 10; 12.5; 15; 17.5; 20; 22.5; 25; 27.5; 30\}$ cm axial positions.

Once again, neutron scattering is impacted by molecular arrangements in water, thus the S(α,β) data associated with water at 300 K have been used in calculations.

Fig. 5 illustrates the two-dimensional variation of $Y_n(r,z)$ as a function of r and z. The drop of neutron response with distance to the source can be observed. By observing the projections of $Y_n(r,z)$ along the r- and z-axes, it also appears that the trends are not rigorously symmetric, so that no separation of variables r and z is allowed.

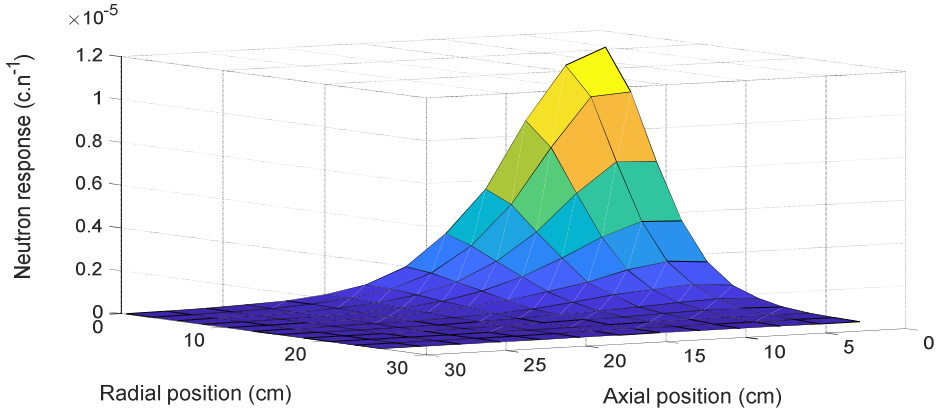

Fig. 5. Evolution of simulated $Y_n(r,z)$ neutron response with respect to r and z distances.

Though the data matrix associated with this profile is sufficient to compute a projector matrix as used in a ML-EM algorithm (Section V), an explicit and continuous fit of the simulation-obtained $Y_n(r,z)$ values will allow the definition of such a projector with an arbitrary discretization. From Fig.5, it can be seen that $Y_n(r,z)$ differs from a decreasing exponential distribution at small r and z values, due to the least portion of water-thermalized neutrons at such distances. Indeed, as position $(0;0)$ corresponds to the center of mass of the FC active part, small values of r and z are mapping the inside of the FC, in which neutrons are less efficiently moderated than in water, or partially captured by cover materials. As a result, we fitted the simulated values with a two-dimensional polynomial function $Y_{\mathrm{fit}}(r,z)$, which is a truncated limited expansion of the exponent:

$$Y_{\mathrm{fit}}(r,z) = \sum_{(i,j)=(0,0)}^{(6,6)} \omega_{ij} r^i z^j \quad (6)$$

A robust ($R^2 > 0.998$) interpolation of the simulated outputs was obtained by a least-mean-square algorithm, with parametrizing ω_{ij} coefficients explicited in Table II.

TABLE II. PARAMETERIZING COEFFICIENTS Ω_{ij} OF THE TWO-DIMENSION POLYNOMIAL FIT

Coefficient $j \setminus i$	**0**	**1**	**2**	**3**	**4**	**5**	**6**
0	1,12E-05	2,16E-07	-4,20E-07	5,31E-08	-2,94E-09	7,79E-11	-8,10E-13
1	2,84E-07	4,61E-07	-1,41E-07	1,65E-08	-9,51E-10	2,69E-11	-2,98E-13
2	-3,37E-07	-1,56E-07	5,96E-08	-7,38E-09	4,35E-10	-1,24E-11	1,38E-13
3	3,57E-08	1,85E-08	-7,16E-09	9,02E-10	-5,38E-11	1,55E-12	-1,75E-14
4	-1,65E-09	-1,02E-09	3,91E-10	-4,97E-11	2,99E-12	-8,70E-14	9,84E-16
5	3,65E-11	2,67E-11	-1,01E-11	1,29E-12	-7,82E-14	2,29E-15	-2,60E-17
6	-3,15E-13	-2,68E-13	1,00E-13	-1,29E-14	7,82E-16	-2,30E-17	2,62E-19

The fit of radial (Fig. 6a) and axial (Fig. 6b) dependences of $Y_n(r,z)$ by the explicit impulse function $Y_{\text{fit}}(r,z)$ of Eq. (6) is illustrated below.

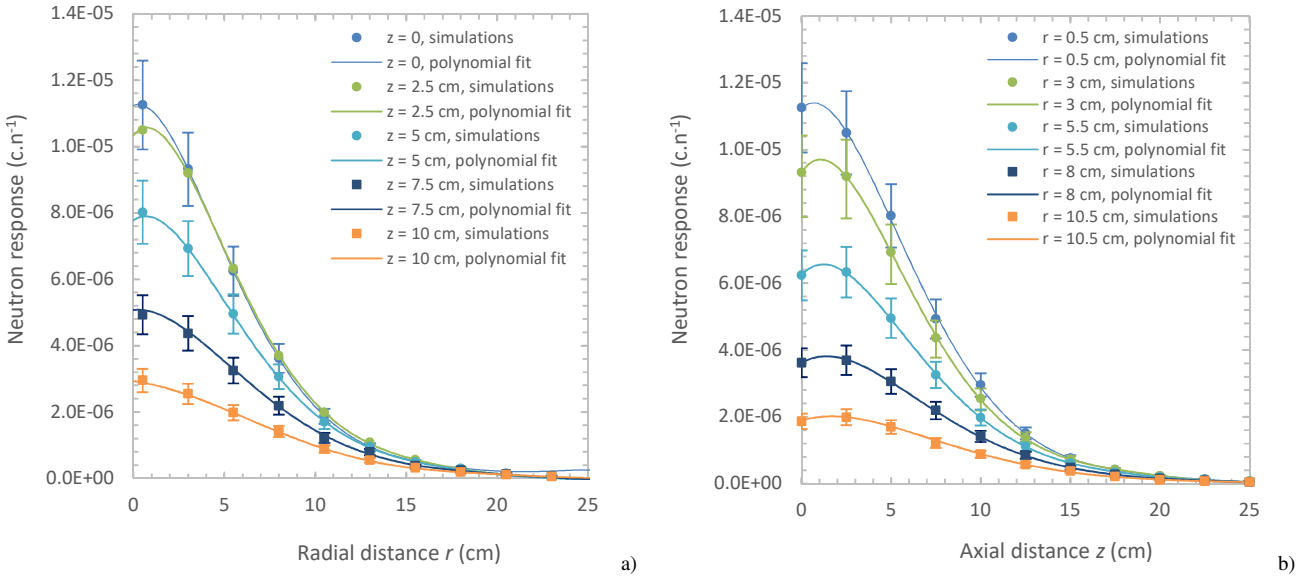

Fig. 6. Evolution of $Y_n(r,z)$ and $Y_{\text{fit}}(r,z)$ as functions of a) radial position r, and b) axial position z.

IV. EXPERIMENTAL STUDY OF A FISSION CHAMBER UNDERWATER: NEUTRON RESPONSE ACCORDING TO AXIAL AND RADIAL AXES

This section is dedicated to the description of the evolution of a CFUE32 FC response $\lambda(r,z)$ (count rate, in cps), set at different positions inside a water drum, as a function of its axial z and radial r distances to a Cf-252 neutron source attached near the center of the container. The experimental study of the influence of a water diffusion environment is indeed of the upmost interest, both to investigate our model of the FC underwater behavior (Section III), and to provide a first set of results in conditions as close as possible to the ones of *in-situ* deployment.

A. *Experimental setup and protocol*

As the parametric experimental study is supposed to reproduce some general features of the *in-situ* deployment environment, a Cf-252, spontaneous fission source, with activity $A = (3.57 \pm 0.12) \cdot 10^4$ Bq at the measurement date, was used. The source was encapsulated in a waterproof, PMMA 3.2 (Ø) × 4.8 cm^3 cylindrical capsule weighted by a $8 \times 2 \times 4.5$ cm^3 lead brick. This ensemble was subsequently placed near the central bottom of a large plastic container, with height $H = 92$ cm, internal radius $R_{int} = 27.5$ cm. The container was eventually filled with water up to $h = 61$ cm from the bottom of the container, and enclosed with a plastic sealing of external radius $R_{ext} = 29$ cm. The sealing was pierced to allow the insertion of the CFUE32 FC, whose inorganic cable, after being enclosed in a plastic holster, was used to mark the position of the FC along the z-axis. Fig. 7a) and b)

respectively present the water-filled container with the Cf-252 neutron source and the sealed container with marks for the referencing the FC position in the (r, z) system.

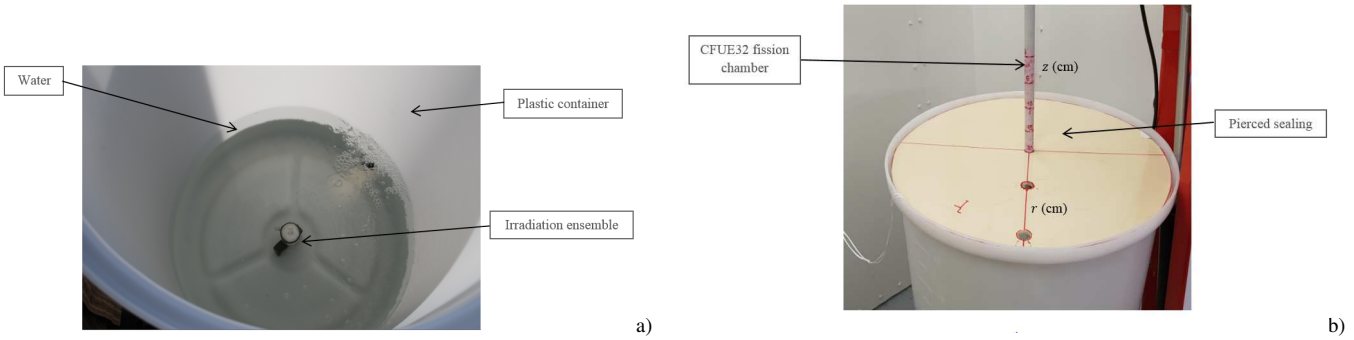

Fig. 7a) Water-filled container with fixed irradiation ensemble at the bottom (Cf-252), and b) sealed container with reference positions along the r and z axes.

The center of the bottom surface of the water-filled container is defined as the *zero position*: $(r, z) = (0; 0)$. The z coordinate is used to designate the axial position of the top of the FC head (11 cm from the center of the sensitive length). The experimental protocol is schematically represented in Fig. 8a) and b), where the subscript "0" refers to the position of the Cf-252 source.

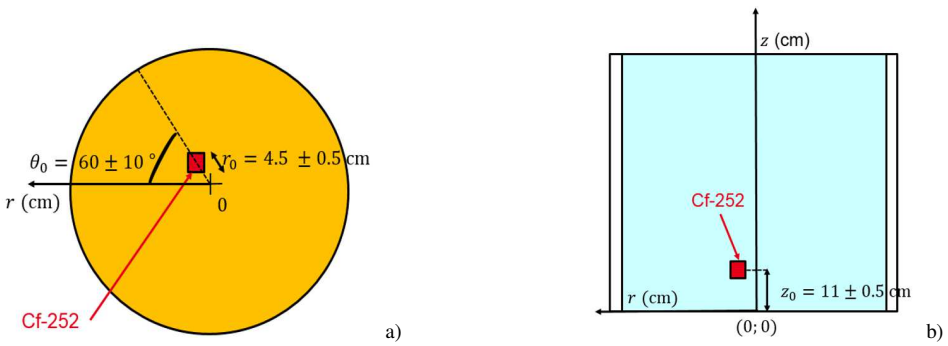

Fig. 8a) Top and b) side schematic view of the experimental protocol.

The plastic tube enclosing the CFUE32 chamber is inserted at three different radial positions $r = \{2; 13; 26\}$ cm. For each of these, neutron countings are recorded at z positions varying between 5 and 30 cm by steps of 5 cm.

B. Experimental response of the CFUE32 FC according to axial and radial distances

To compare radial and axial, experimental distributions with the mathematical adjustment derived in Section III, the acquired neutron count rates $\lambda_n(r, z)$ (cps) are reduced to a neutron yield $\Lambda_n(r, z)$ (c.n^{-1}) using Eq. (1). This yield is then transposed into a new polar system (O', r', z'), where polar coordinates (r', z') respectively correspond to the radial and axial positions of the center of mass of the FC in the spatial system centered in the center of mass of the neutron emitter (O'). Similarly to the simulations detailed *supra*, the lead and PMMA insertion ensemble were scaled so that, at position $z = 0$, the centers of mass of both the FC and the Cf-252 source would be axially aligned (with ± 1 cm spatial uncertainty), so that

$$z' = z \quad (7)$$

The radial position r of the FC is converted into a radial distance r' to the center of mass of the Cf-252 source using the law of cosines (as understandable from the schematic representation in Fig. 8a):

$$r'^2 = r^2 + r_0^2 - 2r \cdot r_0 \cdot \cos(\theta_0) \quad (8)$$

The obtained distributions for $\Lambda_n(r', z')$ are subsequently compared with the fitted impulse function $Y_{\text{fit}}(r', z')$. Although the uncertainties regarding 2D-position and Poisson statistics are large, we found that, over the 18-point set of measured values, $\Lambda_n(r', z')$ are all compatible with $Y_{\text{fit}}(r', z')$ within $\pm 2\sigma\big(\Lambda_n(r', z')\big)$ (second order uncertainty rectangle). The distributions of $\Lambda_n(z')$ and $Y_{\text{fit}}(z')$ are plotted against each other in Fig. 9a) for $r = 2$ cm ($r' = 3.9$ cm), and $r = 13$ cm ($r' = 11.4$ cm). Similarly $\Lambda_n(z')$ and $Y_{\text{fit}}(z')$ profiles are shown in Fig. 9b). In both cases, we observe a quasi-exponential decrease of neutron counting after a few-centimeter range in water.

We may therefore conclude that the impulse response function model Y_{fit} allows for an accurate expectation of the trends and orders of magnitude followed by the signal collected underwater.

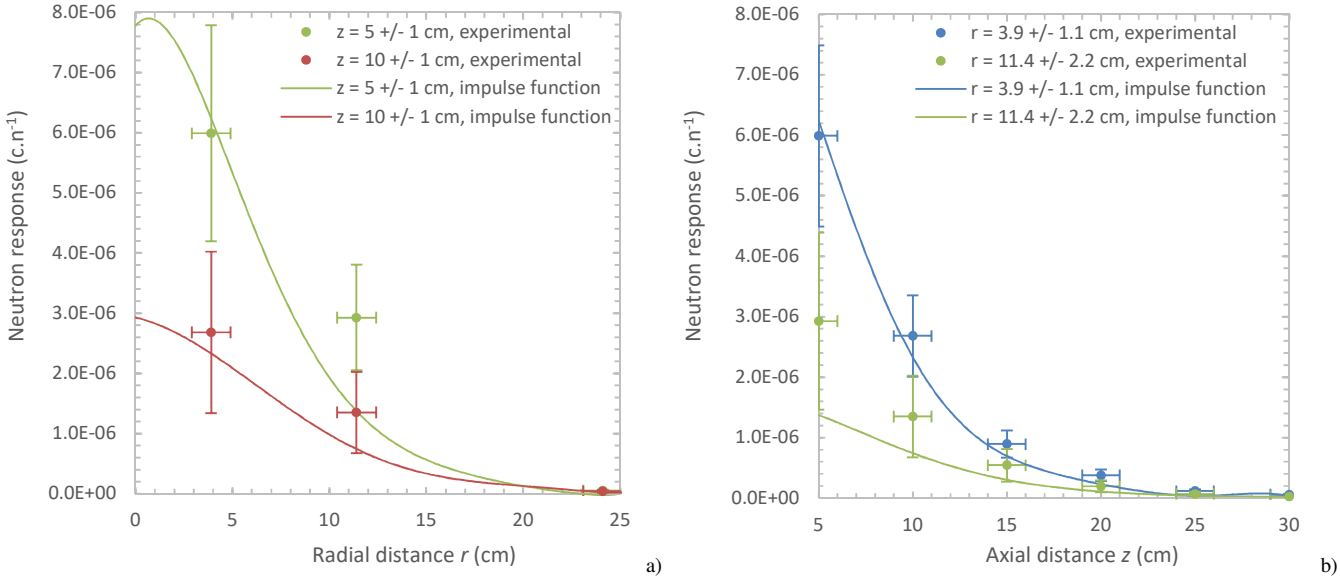

Fig. 9. Evolution of $\Lambda_n(r', z')$ and $Y_{\text{fit}}(r', z')$ as functions of a) radial distance r', and b) axial distance z' (one standard deviation uncertainties).

V. Localization by inverse problem approach: methodology and performance with simulated data

In this last section, we present an approach in which fuel debris localization is defined as an Inverse Problem, solvable with a Maximum-Likelihood Expectation Maximization (ML-EM) iterative algorithm. Such approaches have been used, over the last decades, for as diverse applications as emission tomography or the decoding of gamma-ray pictures obtained with coded-aperture gamma cameras [12,13], and found to allow a refined localization of a radiological source term when Poisson statistics are at play.

A. *Localization by Inverse Problem approach: principle and methodology*

Let λ_i be the i^{th} recorded count rate at a given (r, z) position of the FC relatively to the source, and resulting from the contribution of N regions of interest defined inside the three-dimensional water environment (such regions being referred to as voxels). The core of the methodology lies in writing λ_i as:

$$\forall\, i \in [\![1; P]\!],\ \lambda_i = \sum_{j=1}^{N} y_{ij} a_j \quad (9)$$

with a_j the neutron activity in the j^{th} voxel, and y_{ij} the detection yield for a neutron emitted in the j^{th} voxel at the i^{th} measurement position. Considering a set of P measurement data, corresponding to acquisitions at different positions in the underwater environment, the complete set of equations is written as:

$$\begin{pmatrix} \lambda_1 \\ \vdots \\ \lambda_P \end{pmatrix} = \begin{pmatrix} y_{11} & \cdots & y_{1N} \\ \vdots & \ddots & \vdots \\ y_{P1} & \cdots & y_{PN} \end{pmatrix} \cdot \begin{pmatrix} a_1 \\ \vdots \\ a_N \end{pmatrix} \quad (10)$$

condensed in the matricial form:

$$\Lambda = Y \cdot A \quad (11)$$

The $Y = [y_{ij}]_{i \in [\![1;P]\!], j \in [\![1;N]\!]}$ projector matrix is built by capitalization on the results of Sections III and IV.

Now because of the statistical fluctuations intrinsic to counting measurements, the Inverse Problem of Eq. (11) cannot be solved by a mere inversion of the Y matrix. For this reason, the implementation of an iterative Maximum-Likelihood/Expectation-Maximization (ML-EM) algorithm is the reference approach for solving this inverse problem while

taking nuclear counting, Poisson statistics into account [14-17]. ML aims at finding the matrix A maximizing the likelihood function $\mathcal{L}(\Lambda|A)$, *i.e.* the voxel neutron activities providing the best agreement with observed count rates.

The size and definition of the voxel map is set by end-users, and the number P of measurements positions does not need to equal the number of voxels N. From the impulse response of Eq. (6), arbitrary activity voxels can be built, and their contribution to a counting measurement at a given (x, y, z) position (with $x^2 + y^2 = r^2$) may be derived. In the rest of this section, no voxel extension along the axial direction will be considered: voxels will thus be defined at the bottom of water container with $(\tilde{x}, \tilde{y})$ distances to the center. The voxel plane is discretized as squares of side R. The distance z is taken from the bottom of the container to the center of mass of the FC active area. As an illustration, the neutron activity-normalized contribution to the measurement from an activity square center on $(0; 0; 0)$ would read

$$Y_{\text{fit}}(x, y, z) = \int_{\tilde{x}=-\frac{R}{2}}^{\frac{R}{2}} \int_{\tilde{y}=-\frac{R}{2}}^{\frac{R}{2}} \sum_{(i,j)=(0,0)}^{(6,6)} \omega_{ij} \left(\sqrt{(x-\tilde{x})^2 + (y-\tilde{y})^2}\right)^i z^j \delta(\tilde{x})\delta(\tilde{y}) d\tilde{x} d\tilde{y} \quad (12)$$

In the frame of this study, we ran ML-EM reconstructions with various axial distances z and in configurations where $P > N$.

B. Performance with simulated data

We consider a configuration where the number of measurements P is significantly higher than the number of voxels N. The measurement grid is based on 81 measurements, regularly spaced by 2.5 cm along the x and y axes. Limits of the measurement grid are the following: $x \in [-10; 10]$ cm, $y \in [-10; 10]$ cm. The reconstruction grid is based on 16 activity voxels, regularly spaced by 5 cm, with limits: $\tilde{x} \in [-10; 10]$ cm, $\tilde{y} \in [-10; 10]$ cm. Figure 10a) represents the measurement and reconstruction grids adopted in this study, with the convention for labelling measurement positions (red) and voxels (blue and black): along y-lines from the top left-hand corner. Figure 10b) illustrates the numerical results for $Y \cdot A$ (in cps) obtained for a configuration where a uniform neutron source of activity $A = 10^4$ n.s^{-1} is present in voxels 10 and 16, and axial distance $z = 10$ cm. This activity was chosen because it induces, at $z = 10$ cm, a thermal neutron flux in the order of 10 n.cm^{-2}.s^{-1}, hence in the middle of the target range specified in Section I.

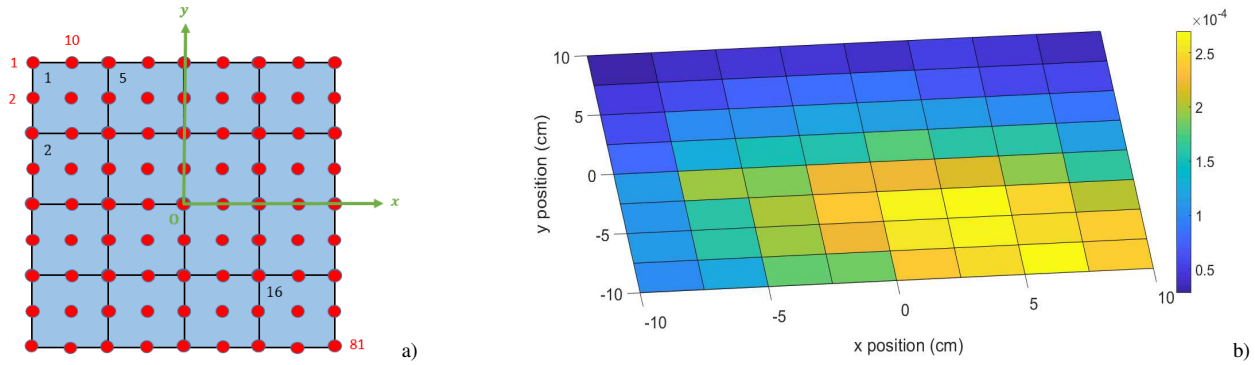

Fig. 10.a) Measurement (red) and reconstruction (blue) grid in the (x, y) plane, and b) $Y \cdot A$ grid corresponding to 10^4 n.s^{-1} neutron sources in voxels 10 and 16.

A vector of simulated counts $(N_i)_{i\in[\![1;P]\!]}$ is generated by sampling the $Y \cdot A$ matrix with Poisson law $\mathcal{P}$:

$$\forall\, i \in [\![1; P]\!],\ N_i \sim \mathcal{P}\left(\left|\left(Y \cdot A \cdot t_{acq}\right)_i\right|\right) \quad (13)$$

with t_{acq} the acquisition at each N measurement point. Figures 10a) and b) illustrate the activity voxel grids, reconstructed after ML-EM analysis over 50.000 iterations (sufficient to ensure convergence with 0.01 %). For acquisition times $t_{acq} = 10$ min, and $t_{acq} = 24$ h, the results are found in agreement with expected voxel configurations. For $t_{acq} = 24$ h, the reconstructed voxels of interest almost perfectly match 10^4 n.s^{-1} source definitions in voxels 10 and 16. Once again, this result is obtained for a sampling of the $Y \cdot A$ matrix, and any significant bias of the response with respect to the said matrix would have induced a more significant discrepancy after reconstruction.

To allow a quantitative assessment of ML-EM performance, we define factors of merit with respect to the accuracy of estimated neutron activities, and the spatial resolution of localized hot spots. The total relative accuracy, labeled RA_{tot} and expressed in %, is the ratio of the estimated total activity over the voxel grid $\widehat{A_{tot}}$, and the known total simulated activity $A_{tot} = 2 \cdot 10^4$ n.s^{-1}. For $t_{acq} \geq 1$ min, two activity clusters are identifiable (two or two couples of adjacent voxels with estimated

activities $\hat{A} > 5 \cdot 10^3$ n.s^{-1}). For both of these clusters, labeled $k \in \{1,2\}$, we also compute, over the voxels enveloping 95 % of the cluster activity, a relative accuracy $R\widehat{A_{k,95\,\%}}$ and spatial resolution $SR_{k,95\,\%}$, given by the summed surface of the said voxels. For our test configuration, the evolution of these factors of merit as a function of t_{acq} is given in Table III. The results show that an Inverse Problem approach allows a fast (1-10 min per point) quantification, within an order of magnitude, and localization, within 100 cm^2, of neutron activity It also gives access to a fine quantification, within 1 %, and localization (25-50 cm^2) of fuel debris for higher acquisition times (> 10 h).

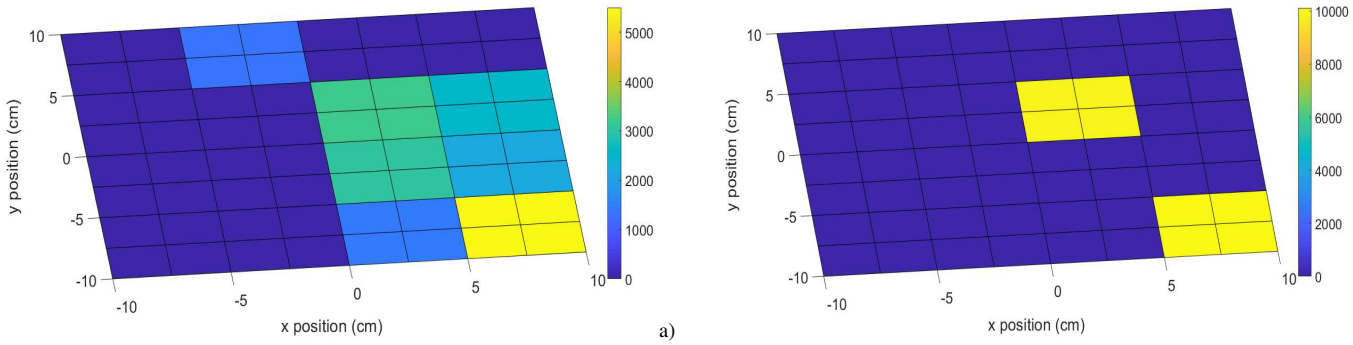

a)

b)

Fig. 11. Reconstruction grids of neutron activities with a) $t_{acq} = 10$ min, and b) $t_{acq} = 24$ h with ML-EM (50.000 iterations).

TABLE III. FACTORS OF MERIT OF LOCALIZATION WITH ACQUISITION TIME

Acquisition time \ Factor of Merit	$\widehat{RA_{tot}}$	$\widehat{RA_{1,95\,\%}}$	$SR_{1,95\,\%}$	$\widehat{RA_{2,95\,\%}}$	$SR_{2,95\,\%}$
30 s	41 %	-	400 cm^2	-	400 cm^2
1 min	26 %	7 %	200 cm^2	60 %	100 cm^2
10 min	4 %	10 %	200 cm^2	3 %	75 cm^2
1 h	1 %	7 %	175 cm^2	8 %	50 cm^2
2 h	1 %	6 %	175 cm^2	6 %	50 cm^2
10 h	1 %	6 %	75 cm^2	8 %	50 cm^2
24 h	0,3 %	1 %	25 cm^2	1 %	25 cm^2

The factors of merit, which were obtained for a thermal neutron flux of 10 n.cm^{-2}.s^{-1}, can additionally be extrapolated to all fluxes in the target range by proportionality.

VI. CONCLUSION

As a conclusion, we described in this article the fundamental building blocks of a model matrix for the definition and solution of fuel debris localization as an Inverse Problem. Experimental campaigns were conducted to validate and calibrate this simulation-based model. The choice of fission-chamber-based technological solution to address the Fukushima-Daiichi issue was consequently highlighted. Parallel work was devoted to the incorporation of a multiple-layer corium model, together with the evaluation of potential losses in FC response to neutrons emitted by fuel debris covered by sediments. We also explored some options for the design of customized FC in view of *in-situ* deployments. Finally, refined versions of the reconstruction algorithm, including MAP-EM algorithms using *a priori*, are under study.

ACKNOWLEDGEMENTS

The authors thank Mitsubishi Research Institute, Inc., for funding this research.

REFERENCES

[1] D. H. Beddingfield, N. H. Johnson, H. O. Menlove, "^{3}He neutron proportional counter performance in high gamma-ray dose environments ", *Nuclear Instruments and Methods in Physics Research A*, Vol. 455, pp. 670-682 (2000).

[2] P. Filliatre, C. Jammes, L. Oriol, B. Geslot, L. Vermeeren, "Monitoring the fast neutrons in a high flux: the case for ^{242}Pu fission chambers", *Proceedings of 2009 First International Conference on Advancements in Nuclear Instrumentation Measurement Methods and their Applications* (2009).

[3] https://www.photonis.com/en/product/fission-chambers-core-use
[4] S. A. Enger, P. Munck af Rosenschöld, A. Rezaei, H. Lundqvist, "Monte Carlo calculations of thermal neutron capture in gadolinium: A comparison of GEANT4 and MCNP with measurements", *Medical Physics*, Vol. 33, N° 2, pp. 337-341 (2006).
[5] D. B. Pelowitz (Ed.), *MCNP6™ User's Manual Version 1.0*, Los Alamos National Laboratory report, LA-CP-13-00364, Rev. 0 (2013).
[6] http://datasheets.globalspec.com/ds/316/PHOTONIS/96A95D08-3367-4CCF-8507-4AF01EB885EC
[7] *Moritz Geometry Tool, Version 1.23, An Interactive Geometry Editor/Viewer for MCNP and MCNPX*, White Rock Science, Los Alamos, New Mexico (2012).
[8] U. Pujala, L. Thilagam, T. S. Selvakumaran, D. K. Mohapatra, E. Alagu Raja, K. V. Subbaiah, R. Baskaran, "Analysis of neutron streaming through the trenches at linac based neutron generator facility, IGCAR", *Radiation Protection and Environment*, Vol. 34, pp. 262-266 (2011).
[9] K. Anderson, J. Pilcher, H. Wu, *Neutron Irradiation Tests of an S-Link-over-G-Link System*, ATLAS Tile Calorimeter internal document (1999).
[10] M. Ben Mosbah, *Spectrométrie des neutrons : étude de la réponse d'un ensemble de compteurs proportionnel*, Thèse de Doctorat, Université de Franche-Comté, pp. 15-16 (2005).
[11] R. Radev, T. McLean, *Neutron sources for standard-based testing*, Technical Report LLNL-TR-664160, Lawrence Livermore National Laboratory (LLNL), Livermore, CA, United States (2014).
[12] W. Lee, D. Wehe, "3D position of radiation sources using an automated gamma camera and ML algorithm with energy-dependent response functions", *Nuclear Instruments and Methods in Physics Research A*, Vol. 531, pp. 270-275 (2004).
[13] F. Carrel, R. Abou Khalil, S. Colas, D. de Toro, G. Ferrand., E. Gaillard-Lecanu, M. Gmar *et al*., "GAMPIX: a New Gamma Imaging System for Radiological Safety and Homeland Security Purposes", *Proceedings of the IEEE Conference/RTSD workshop* (2011).
[14] H. O. Hartley, "Maximum Likelihood Estimation from Incomplete Data", *Biometrics*, Vol. 14, pp. 174-194 (1958).
[15] A. P. Dempster, N. M. Laird, D. B. Rubin, "Maximum Likelihood from Incomplete Data via the EM Algorithm", *Journal of the Royal Statistical Society*, Vol. 39, pp. 1-38 (1977).
[16] L. A. Shepp, Y. Vardi, "Maximum Likelihood Reconstruction for Emission Tomography", *IEEE Trans. Med. Imaging*, Vol. 1, pp. 113-122 (1982).
[17] H. Lemaire, E. Barat, F. Carrel, T. Dautremer, S. Dubos, O. Limousin, T. Montagu, S. Normand, V. Schoepff, K. Amgarou, N. Menaa, J.-C. Angélique, A. Patoz, "Maximum Likelihood Expectation-Maximization algorithms applied to localization and identification of radioactive sources with recent coded mask gamma cameras", *Proceedings of 2015 4th International Conference on Advancements in Nuclear Instrumentation Measurement Methods and their Applications* (2015).